

Hodge Decomposition of Wall Shear Stress Vector Fields characterizing Biological Flows

Faniry H. Razafindrazaka^{1,2}, Pavlo Yevtushenko², Konstantin Poelke¹, Konrad Polthier¹, and Leonid Goubergrits²

¹*Freie Universität Berlin, Germany*

²*Institute for Imaging Science and Computational Modelling in Cardiovascular Medicine, Charité-Universitätsmedizin Berlin, Germany*

Abstract

A discrete boundary-sensitive Hodge decomposition is proposed as a central tool for the analysis of wall shear stress (WSS) vector fields in aortic blood flows. The method is based on novel results for the smooth and discrete Hodge-Morrey-Friedrichs decomposition on manifolds with boundary and subdivides the WSS vector field into five components: gradient (curl-free), co-gradient (divergence-free), and three harmonic fields induced from the boundary, which are the center harmonic, Neumann and Dirichlet fields. First, an analysis of WSS in several simulated simplified phantom geometries (duct and idealized aorta) was performed in order to understand the impact of the five components. It was shown that the decomposition is able to distinguish harmonic blood flow arising from the inlet from harmonic circulations induced by the interior topology of the geometry. Finally, a comparative analysis of 11 patients with coarctation of the aorta (CoA) before and after treatment as well as 10 controls patient was done.

The study shows a significant difference between the CoA patients and the healthy controls before and after the treatment. This means a global difference between aortic shapes of diseased and healthy subjects, thus leading to a new type of WSS-based analysis and classification of pathological and physiological blood flow.

Keywords: Hodge decomposition, vector fields, wall shear stress, computational fluid dynamics, coarctation of the aorta

1 Introduction

Biological flows or hemodynamics of cardiovascular system play an important role in the genesis, progress and treatment of cardiovascular pathologies including congenital or acquired diseases of heart, heart valves and vessels. This is because wall remodeling including wall thickness and wall constitution is triggered

by hemodynamics. The major hemodynamic parameter describing an interaction between hemodynamics and a vessel wall, which is covered by endothelial cells, is the wall shear stress (WSS). The WSS is an area-normalized tangential force component of the blood flow acting on the wall and/or endothelial cells. In turn, endothelial cells trigger and modulate adaptation, inflammation and remodeling of the vessel wall as well as a respective remodeling of the vessel lumen [1, 2]. Consequently, WSS is considered as an important local risk factors for a set of diseases or pathological processes. These include, for example, atherosclerosis of carotid arteries [3] or coronary artery disease [4], rupture risk of cerebral aneurysms [5, 6] or abdominal aortic aneurysms [7], aortic dilatation [8], and thrombus formation [9]. Furthermore, the analysis of the WSS is also of great interest for the study of the hemodynamic impact of a treatment or a change of the hemodynamics caused by a used treatment device. These studies include, for example, an analysis of post-treatment flow conditions after a treatment of cerebral aneurysms with flow diverter [10] or a change of flow conditions after an aortic valve replacement [11]. The use of the WSS as a reliable biomedical marker characterizing disease, disease progress or initiation and also characterizing hemodynamic outcome of a treatment procedure is challenging. This is because WSS is a surface bounded vector field that means that WSS is described by a magnitude and direction varying in space and time. This allows a definition of a set of parameters, which were proposed during last years as hemodynamic risk parameters for endothelial dysfunction and related wall remodeling. A characterization of WSS magnitude, direction, time and space gradients as well as topological features results in a relatively large set of parameters, which are well summarized in [12] and [13]. The majority of studies investigating WSS in biological flows are numerical studies investigating hemodynamics by an image-based computational fluid dynamics approach [14]. 4D VEC MRI based assessment of the WSS is also proposed in [15]. The primary source of data for the WSS analysis, however, is CFD, since accurate WSS assessment requires high spatial resolution as shown by mesh independence studies for CFD solutions [16].

Vector fields modelling fluid flow often tend to exhibit a complicated behaviour on various scales and are hard to understand. This poses a particular problem for clinical applications where the behaviour of blood flow in vessels serves as an indicator for potential abnormalities. The classical Helmholtz decomposition was a first step to classify and analyse vector fields by decomposing them into a divergence-free component and a component having a potential. With the advent of Hodge theory, Helmholtz' results generalize to decomposition rules for differential forms on closed manifolds in arbitrary dimensions. Since then a tremendous amount of research—both on the theoretical and on the applied side—has been carried out to include manifolds with boundary, differential forms of Sobolev class and various flavours of Hodge-type decomposition statements, see e.g. [17] for an overview of Hodge-type decompositions and the survey [18].

An important landmark in this evolution is the L^2 -orthogonal decomposition

of k -forms on manifolds with boundary as

$$\Omega^k = d\Omega_D^{k-1} \oplus \delta\Omega_N^{k+1} \oplus d\Omega^{k-1} \cap \delta\Omega^{k+1} \oplus (\mathcal{H}_N^k + \mathcal{H}_D^k)$$

where the spaces \mathcal{H}_N^k and \mathcal{H}_D^k of harmonic Neumann and Dirichlet fields, respectively, reflect the absolute and relative cohomology of the manifold. Specifically for vector fields, the first two spaces in this decomposition correspond to divergent and rotational irregularities in the interior of the geometry, whereas the latter three spaces represent steady flows through the domain, as each field in these spaces is harmonic. A recent result [19] provides a further orthogonal decomposition of these spaces into subspaces

$$\mathcal{H}_N^k = \mathcal{H}_{N,\text{co}}^k \oplus \mathcal{H}_{N,\partial\text{ex}}^k \quad \text{and} \quad \mathcal{H}_D^k = \mathcal{H}_{D,\text{ex}}^k \oplus \mathcal{H}_{D,\partial\text{co}}^k$$

which permits a precise distinction between harmonic flows induced by boundary components, represented by the subspaces $\mathcal{H}_{N,\text{co}}^k$ and $\mathcal{H}_{D,\text{ex}}^k$, from those induced by the interior topology of the manifold, represented by $\mathcal{H}_{N,\partial\text{ex}}^k$ and $\mathcal{H}_{D,\partial\text{co}}^k$.

For the numerical treatment of vector fields it is therefore important to seek for a discretization which on the one hand provides a good approximation with predictable error, and on the other hand preserves the structural decomposition results from the smooth theory.

In this research paper, we focus on a discretization by piecewise constant vector fields (PCVF) resulting from CFD based analysis of the blood flow. PCVFs are a very intuitive and simple to implement approximation while at the same time a concise theoretical framework has been developed in recent years, which includes the aspects of convergence and structural consistency. The recent work [24, 28] establishes a consistent discretization for PCVFs of the smooth refined decomposition results for vector fields on surfaces with boundary, now including distinguished subspaces for effective boundary analysis and control. Previous to that, a first strategy for the analysis of vector fields is provided by the decomposition in [21], with a convergence analysis on closed surfaces in [22], and a discrete connection for PCVFs is proposed in [23], both without an effective boundary control.

The aim of our study presented here is a proof of concept for the novel Hodge-type decomposition analysis of the WSS vector fields for blood flows in general and specifically for the aortic flow. The paper is structured as follows: first, a theoretical background on the discrete Hodge-type decomposition together with an interpretation of each component with respect to a WSS vector field is given. Second, a detailed description of the data acquisition and blood flow simulation is exposed. Finally, a statistical analysis of several patients will summarize the new results.

2 Theoretical Background

In this section, we give a brief introduction of calculus on discrete surfaces. Only the most relevant notions in order to understand the discrete Hodge decomposition are given. A complete overview can be found in [21].

2.1 Simplicial Surfaces

A 2-dimensional *simplicial surface* M_h is a set of triangles glued at their edges with a manifold structure. In finite element analysis, this type of discrete surface is called *triangle mesh*. For actual FEM computations on such meshes one often uses the space S_h of linear Lagrange functions, or the space S_h^* of Crouzeix-Raviart functions. They are defined by

$$S_h := \{ \varphi : M_h \rightarrow \mathbb{R} \mid \varphi|_T \text{ is linear on each triangle } T, \text{ and globally continuous} \}$$

$$S_h^* := \{ \psi : M_h \rightarrow \mathbb{R} \mid \psi|_T \text{ is linear, and continuous at edge midpoints} \}$$

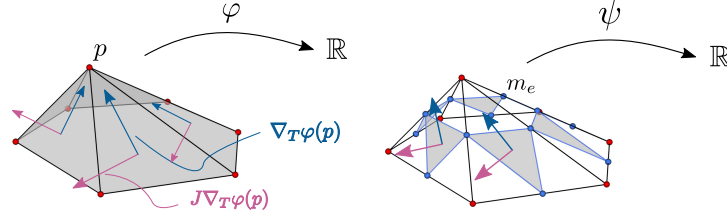


Figure 1: Examples of a function $\varphi \in S_h$ together with $\nabla \varphi$, $J\nabla \varphi$ (left) and $\psi \in S_h^*$ with $\nabla \psi$, and $J\nabla \psi$ (right) defined over the triangle T .

A geometric realization of example functions on S_h and S_h^* is shown in figure 1. Two additional subspaces $S_0 \subset S_h$ and $S_0^* \subset S_h^*$ for surfaces with boundary are given by

$$S_0 := \{ \varphi \in S_h \mid \varphi(v) = 0 \text{ for all boundary vertices } v \}$$

$$S_0^* := \{ \psi \in S_h^* \mid \psi(m_e) = 0 \text{ for all boundary edge mid-points } m_e \}.$$

The *gradient field* $\nabla \varphi$ of a function $\varphi \in S_h$ or S_h^* is a constant tangent vector in each triangle. The *co-gradient field* $J\nabla \varphi$ is obtained by a rotation J of the gradient $\nabla \varphi$ by $\frac{\pi}{2}$ in each triangle (see figure 1). The idea of having functional spaces is a common technique in finite element analyses to solve complicated partial differential equations. For example a temperature map u which assigns a scalar value to each vertex of M_h is an element of S_h . It can be expressed with respect to the nodal basis functions $(\varphi_i)_i$ of S_h , i.e $u = \sum_i u_i \varphi_i$, where φ_i is the Kronecker delta, $\varphi_i(v_j) = 1$ if $i = j$ and 0 otherwise, for a vertex v_j of M_h . Then, the gradient of an arbitrary function in S_h can simply be expressed as a linear combination of the $\nabla \varphi_i$'s.

2.2 Vector fields on Simplicial Surfaces

Definition 2.1 (PCVF) *The space of piecewise constant tangential vector fields $\Lambda^1(M_h)$ on a 2-dimensional simplicial surface $M_h \subset \mathbb{R}^n$ is given by:*

$$\Lambda^1(M_h) := \{ \mathcal{X} : M_h \rightarrow TM_h \mid \mathcal{X}|_{\text{triangle } T} \text{ is a constant tangent vector in } T \}.$$

Here, TM_h denotes the (piecewise) tangent bundle of M_h . The gradient field $\nabla\varphi$ introduced previously is an example of a tangential vector field.

Definition 2.2 (L^2 -product) *The L^2 -product of two vector fields, $\mathcal{X} = (\mathcal{X}_T)_{T \in M_h}$ and $\mathcal{Y} = (\mathcal{Y}_T)_{T \in M_h}$, where $\mathcal{X}_T, \mathcal{Y}_T$ are tangent vectors in the triangle T , is defined by the area-weighted Euclidean sum*

$$\langle \mathcal{X}, \mathcal{Y} \rangle_{L^2} = \sum_{T \in M_h} \langle \mathcal{X}_T, \mathcal{Y}_T \rangle \text{Area}(T).$$

In particular, two vector fields \mathcal{X} and $\mathcal{Y} \in \mathcal{X}_h$ are L^2 -orthogonal if $\langle \mathcal{X}, \mathcal{Y} \rangle_{L^2} = 0$. A vector field subspace $A \subseteq \Lambda^1(M_h)$ is the L^2 -orthogonal decomposition of two subspaces $B, C \subseteq A$ (written $A = B \oplus C$) if every $\mathcal{X} \in A$ can be written uniquely as a sum $\mathcal{X} = \mathcal{Y} + \mathcal{Z}$ with $\mathcal{Y} \in B$ and $\mathcal{Z} \in C$, and furthermore $\langle \mathcal{Y}, \mathcal{Z} \rangle = 0$. The sum of two vector fields is a new vector field obtained by the sum of the components.

2.3 Discrete Calculus

Definition 2.3 (Discrete Curl) *The discrete curl of a vector field $\mathcal{X} = (\mathcal{X}_T)_{T \in M_h}$ at a vertex p and an edge midpoint m_e of M_h is computed by*

$$\begin{aligned} \text{curl}_h \mathcal{X}(p) &:= \frac{1}{2} \oint_{\partial \text{star } p} \mathcal{X} = \frac{1}{2} \sum_{i=1}^k \langle \mathcal{X}|_{T_i}, e_i \rangle \\ \text{curl}_h^* \mathcal{X}(m_e) &:= \oint_{\partial \text{star } e} \mathcal{X} = -\langle \mathcal{X}|_{T_1}, e \rangle + \langle \mathcal{X}|_{T_2}, e \rangle \end{aligned}$$

where the e_i 's are the edges of the oriented boundary of star p , the T_i 's the triangles adjacent to p and e the edge with midpoint m_e (see figure 2).

Definition 2.4 (Discrete Divergence) *The discrete divergence of a vector field \mathcal{X} at a vertex p and an edge midpoint m_e of M_h is computed by*

$$\begin{aligned} \text{div}_h \mathcal{X}(p) &:= \frac{1}{2} \oint_{\partial \text{star } p} \langle \mathcal{X}, \mathbf{n} \rangle ds = -\frac{1}{2} \sum_{i=1}^k \langle \mathcal{X}|_{T_i}, J e_i \rangle \\ \text{div}_h^* \mathcal{X}(m_e) &:= \oint_{\partial \text{star } e} \langle \mathcal{X}, \mathbf{n} \rangle ds = \langle \mathcal{X}|_{T_1}, J|_{T_1} e \rangle + \langle \mathcal{X}|_{T_2}, J|_{T_2} e \rangle \end{aligned}$$

where \mathbf{n} is the outer unit normal along $\partial \text{star } p$ resp. $\partial \text{star } e$. Discrete rotation and divergence are related by $\text{curl}_h J\mathcal{X} = \text{div}_h \mathcal{X}$ and $\text{curl}_h^* J\mathcal{X} = \text{div}_h^* \mathcal{X}$, compare Figure 2.

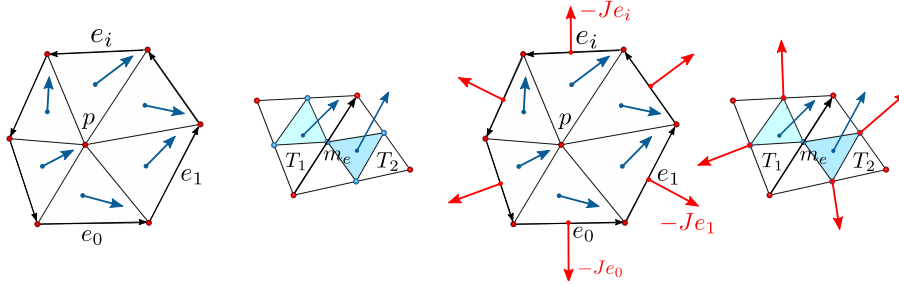


Figure 2: Computation of the curl and divergence of a vector field at a point on ∇S_h and $J\nabla S_h^*$.

Definition 2.5 (Dirichlet and Neumann field) A vector field \mathcal{X} is a Dirichlet field (resp. Neumann field) if $\mathcal{X}|_{T \in \partial M_h}$ is orthogonal (resp. “almost” parallel) to the boundary edge of T .

In the discrete case, the definition of Neumann fields is subtle due to technical properties of the chosen function spaces S_h and S_h^* . They are not strictly parallel along the boundary as one might expect from the smooth case, but can deviate slightly. However, they are overall mostly parallel, so for simplicity one may imagine them as being just parallel, in perfect duality to the definition of Dirichlet fields. For technical details we refer the reader to [24, Sec. 3.1].

The harmonic Dirichlet field \mathcal{H}_D is for example a divergence-free and a curl-free field orthogonal to ∂M_h . Note that Dirichlet fields and Neumann fields do not exist on a closed surface. One can nevertheless define them using hard directional constraints on certain features of the underlying surface, e.g sharp features.

2.4 Discrete Hodge-type Decomposition

Theorem 2.1 (Hodge-Helmholtz decomposition) The space of piecewise constant vector fields $\Lambda^1(M_h)$ on a closed simplicial surface M_h decomposes into an L^2 -orthogonal sum of the spaces of gradient fields, co-gradient fields and harmonic fields:

$$\Lambda^1(M_h) = \nabla S_h \oplus J\nabla S_h^* \oplus (H := \ker \text{curl}_h^* \cap \ker \text{div}_h)$$

$$\mathcal{X} = \underbrace{\nabla \varphi}_{\text{curl}_h^* \nabla \varphi = 0} \oplus \underbrace{J\nabla \psi}_{\text{div}_h J\nabla \psi = 0} \oplus \underbrace{\mathcal{Y}}_{\text{curl}_h^* \mathcal{Y} = \text{div}_h \mathcal{Y} = 0}$$

Fields belonging to ∇S_h are free of turbulence and contain only flow induced by sources and sinks. $J\nabla \psi$ is divergence-free and contains the rotational part of the field. Furthermore, if M_h is homeomorphic to a sphere with m boundaries, then the harmonic fields can be decomposed into three components.

Theorem 2.2 (Hodge-Morrey-Friedrichs decomposition HMF) On a surface M_h homeomorphic to a sphere with m boundaries, the space of harmonic

fields can be decomposed into Neumann fields, center fields, and Dirichlet fields:

$$\begin{aligned}\Lambda^1(M_h) &= \nabla S_0 \oplus J\nabla S_0^* \oplus H_N \oplus \nabla S_h \cap J\nabla S_h^* \oplus H_D \\ \mathcal{X} &= \nabla\varphi \oplus J\nabla\psi \oplus \mathcal{H}_N \oplus \mathcal{H}_C \oplus \mathcal{H}_D\end{aligned}$$

One of the main studies of this paper is to understand the nature of these harmonic spaces on simulated CFD vector fields. Intuitively the space $\nabla S_h \cap J\nabla S_h^*$ behaves similarly to the space of smooth vector fields forming an $\approx 45^\circ$ angle with the boundaries. By the Pythagorean theorem it is

$$\|\mathcal{X}\|^2 = \|\nabla\varphi\|^2 + \|J\nabla\psi\|^2 + \|\mathcal{H}_N\|^2 + \|\mathcal{H}_C\|^2 + \|\mathcal{H}_D\|^2$$

which enables a full quantification of the input vector fields according to their decomposition components. Figure 3 shows an example of a HMF-decomposition on the WSS of an idealized aorta. Notice how the field is dominated by \mathcal{H}_D .

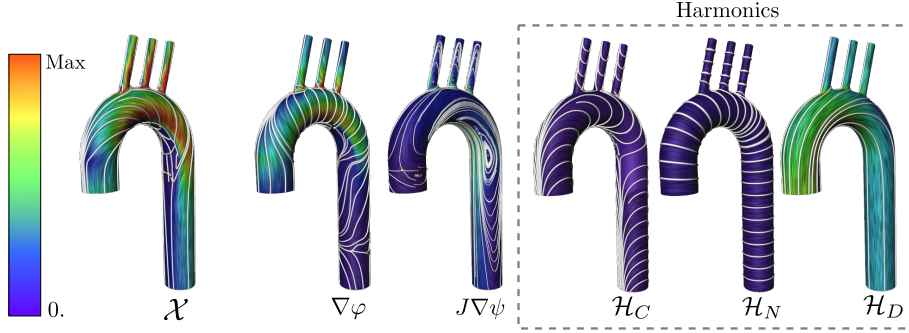


Figure 3: HMF-decomposition of the WSS of an idealized aorta with a constant input velocity profile. The vector field is decomposed into: gradient (34%), co-gradient (11%), harmonic Neumann (0%), harmonic Center (0%), and harmonic Dirichlet (55%). The color encodes the strength of the vector fields, lines show the direction of the flows.

2.5 WSS Component Analysis

In this section, we study each component of the HMF-decomposition with respect to the WSS of phantom models obtained from CFD. The phantom models are either hand-designed or real patient models with mathematical deformation and boundary conditions.

The gradient field $\nabla\varphi$: The gradient field is a curl-free field varying relative to the magnitude of the input velocity profile. In terms of WSS, a high blood velocity induces high $\nabla\varphi$, principally at regions with high curvatures and vessel branches. To validate this assumption, an artificial aorta with varying outlet numbers (from zero to four) have been simulated with plug blood profile. The

results are shown in figure 4. Notice that the increase in $\nabla\varphi$ is amortized by the decrease in \mathcal{H}_D . Evaluated on real patient data, general rules relating the gradient component and the Dirichlet field have not been observed.

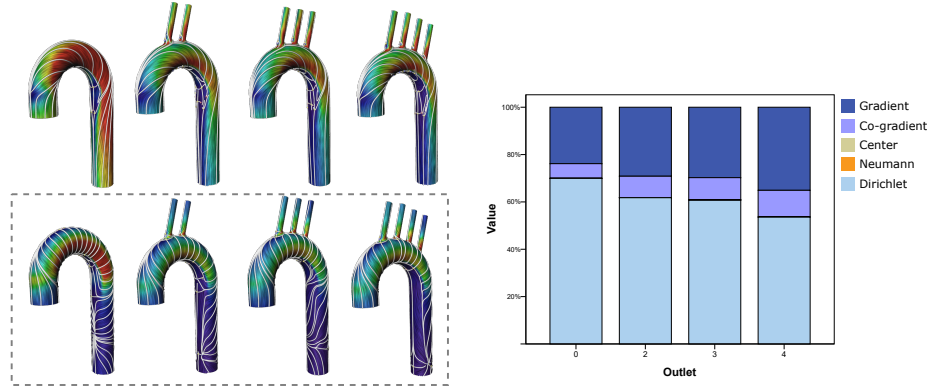


Figure 4: Analysis of artificial aorta models with a varying number of outlets. The second row shows the flow of the gradient field. The diagram shows that the number of branching outlets is closely related to the gradient and Dirichlet field.

The co-gradient field $J\nabla\psi$: The co-gradient field $J\nabla\psi$ is a divergence-free field which changes with respect to the radial variation of each local branch present in the biological model. This component is a very good measure to distinguish evolution of coarctation in aorta before and after a patient intervention. In Figure 5 (right), the smooth deformation between a patient model before and after intervention shows a significant reduction in $J\nabla\psi$ which corresponds to a reduction in turbulence. Notice also how the $\nabla\varphi$ stays invariant where \mathcal{H}_D increases slightly.

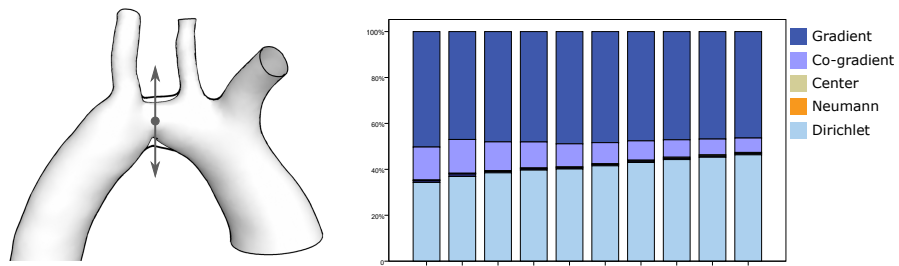


Figure 5: Linear deformation of a pre to post intervention of a patient stenosis. A constant input velocity profile is used for the simulation. A reduction of the co-gradient and hence turbulence is observed from 10 frames of the deformation.

The center \mathcal{H}_C and Neumann field \mathcal{H}_N : These two components are affected generally by the nature of the inlet boundary conditions. Non uniform input velocity profile, example from MRI, tends to increase these components where in a plug profile simulation, they remain negligible. In figure 6 is an example showing that plug profiles produce less \mathcal{H}_C and \mathcal{H}_N than MRI profile. The logic behind this is that in the nature of the HMF-decomposition, \mathcal{H}_C and \mathcal{H}_N are more circulating flow, e.g around cylindrical regions, than axial. Further experiments conducted on several patients have validated this observation. Notice also how \mathcal{H}_D stays invariant.

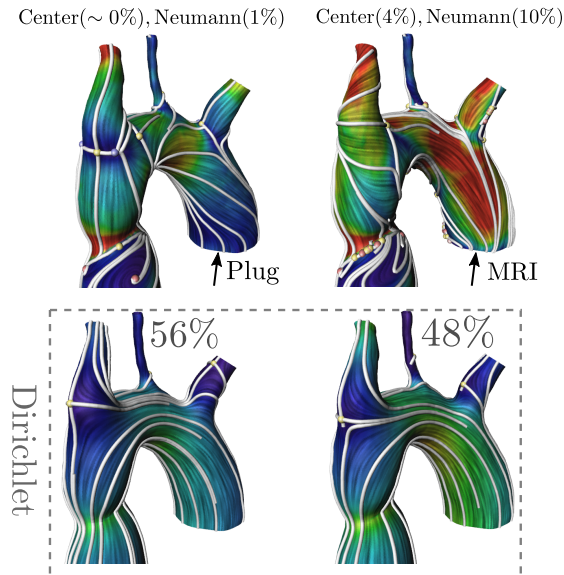


Figure 6: First row: Plug vs MRI input profile encoded in the center and Neumann components. Second row: invariance of the Dirichlet component under the change of input profile.

The Dirichlet field \mathcal{H}_D : To understand the field \mathcal{H}_D , consider a smooth cylinder with a WSS laminar flow. We add a moderate amount of rotational noise to the vector field within the interval $(-\alpha, \alpha)$ where α bounds the frequency of the noise. High values of α correspond to high overall frequencies while small values alter slightly the global smoothness of the flow. The HMF-decomposition shows that \mathcal{H}_D recovers the original field in its unperturbed state, behaving similarly to a vector field denoising. The increase of α decreases \mathcal{H}_D . Figure 7 is a quantitative comparison of each decomposition where α varies from 0° to 90° degree. The diagram shows that \mathcal{H}_D is a good reference to understand the global structure of the WSS. In general, harmonic fields depend only on the topology of the shape, not the field. In figure 6 (second row), for example, \mathcal{H}_D stays invariant even though the input velocity profile is changed.

Quantitatively half of the WSS component is Dirichlet. One logic behind this is reflected in the nature of fluid flows, being mostly dominated by a laminar component in order to only move in one direction.

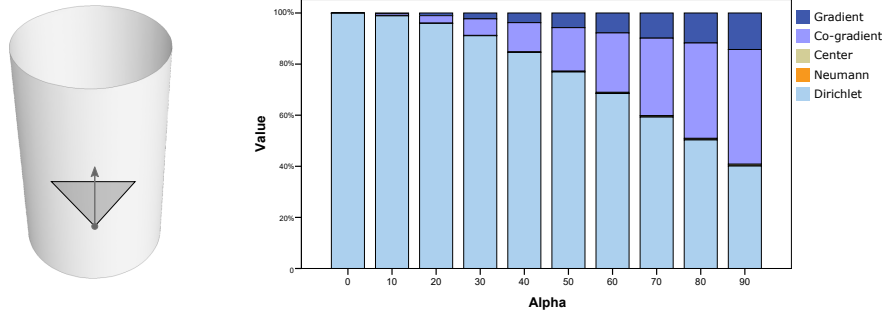


Figure 7: Perturbation of a laminar WSS on a cylinder starting from 0° to 90° . Increase in angle deviation decreases the Dirichlet component.

3 Method

A diagram summarizing the proposed approach is given in figure 8. The implementation of the HMF-decomposition is done following the iterative L^2 -projection approach [21]. The choice of basis functions for each harmonic field subspaces are computed following [24]. Our system takes as input a mesh with a vector field and return the five components decomposition of the vector field, assuming that the surface fulfill the topological requirement. Our implementation is done in Java using the JavaView (www.javaview.de) geometry processing package. The line integral convolution (LIC) implemented in ZIBAmira 2015.28 (Zuse Institute Berlin) is used for the field visualization. Maximum magnitude is colored with red while close to zero vectors are colored in violet. Most of the data used in this paper is from real patient biological models.

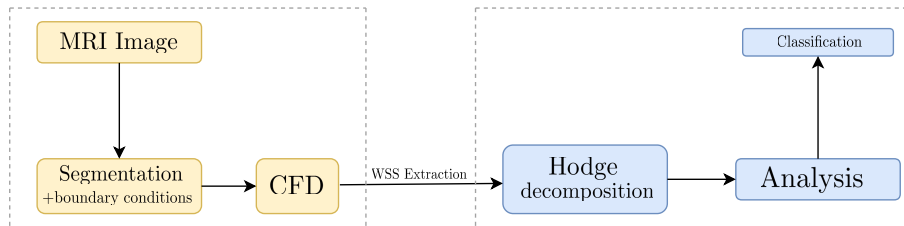


Figure 8: Analysis pipeline of WSS vectors extracted from a simulated model and analyzed through Hodge decomposition.

3.1 Data Input

MRI data: The HMF-decomposition analysis was done for WSS vector fields of the aorta from MRI based CFD analysis of the aortic flow. These are subdivided in two groups: controls and coarctation of the aorta (CoA) patients before and after the treatment.

The study was carried out according to the principles of the Declaration of Helsinki and approved by the local ethics committee. Written informed consent was obtained from the participants and/or their legal guardians.

MRI examinations used to set boundary conditions for CFD analysis were performed using a 1.5 Tesla Achieva R5.1.8. MRI scanner with a five-element cardiac phased-array coil (Philips Medical Systems, Best, The Netherlands). MRI protocols included routine three-dimensional anatomical imaging in end-diastole used to reconstruct the geometry of the aorta (3D MRI). The sequence parameters used were: acquired voxel size $0.66 \times 0.66 \times 3.2$ mm, reconstructed voxel size $0.66 \times 0.66 \times 1.6$ mm, repetition time 4 ms, echo time 2 ms, flip angle 90° , number of signal averages 3. Four-dimensional velocity-encoded MRI (4D VEC MRI) was used to capture flow data of the ascending aorta and the thoracic aorta (acquired voxel size $2.5 \times 2.5 \times 2.5$ mm, reconstructed voxel size $1.7 \times 1.7 \times 2.5$ mm, repetition time 3.5 ms, echo time 2.2 ms, flip angle 5° , 25 reconstructed cardiac phases, number of signal averages 1). High velocity encoding (3-6 m/s) in all three directions was used in order to avoid phase wraps in the presence of valve stenosis or secondary flow. All flow measurements were completed with automatic correction of concomitant phase errors. These data were used to set inflow and outflow boundary conditions.

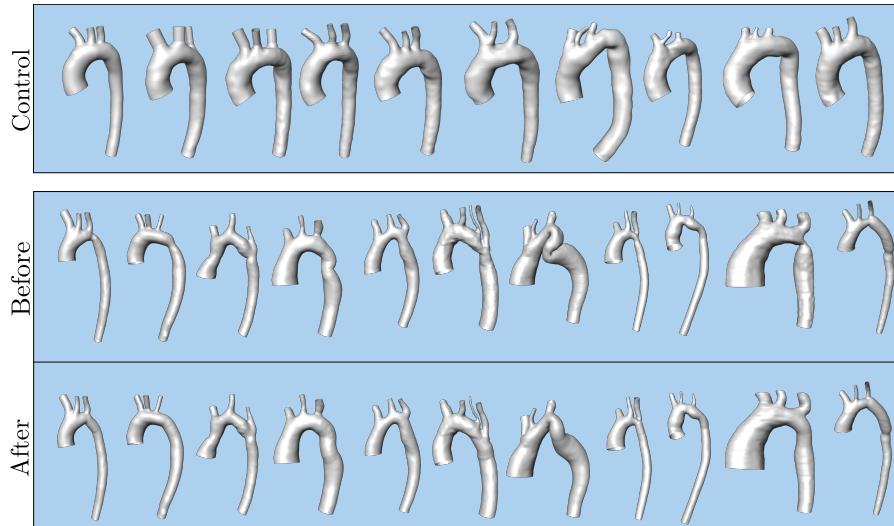


Figure 9: Segmented aorta reconstructed from MRI images and used for the CFD simulation.

CFD data: CFD requires geometries. Geometries of human aortas were segmented and reconstructed using ZIBAmira 2015.28 (Zuse Institute Berlin, Berlin, Germany) according to previous description [25]. Briefly, intensity based image segmentation was done semi-automatically with an intense manual interaction. Rough surface geometries were then generated from segmentations with a subvoxel accuracy and subsequently smoothed using Meshmixer (v. 3.3, Autodesk, Inc., San Rafael, USA). These procedures were described in more details earlier [25]. Figure 9 shows all aorta models used for analysis.

Steady-state simulations of the peak-systolic aortic flow were performed using STAR-CCM+ (v. 12.06, Siemens PLM Software, Plano, USA). Vessel walls were assumed to be rigid and a no-slip boundary condition was applied at all walls. To model turbulence observed in systolic aortic hemodynamics, a $k - \omega$ SST turbulence model with a turbulence intensity of 5 percent at the velocity inlet was used. Blood was modelled as a non-Newtonian fluid with a constant density of 1050 kg/m^3 and a Carreau-Yasuda viscosity model [26]. Patient-specific flow rates as measured with GTFlow (GyroTools LLC, Zurich, Switzerland) from 4D VEC MRI data were set at the LVOT inlet and the descending aorta outlet. Furthermore, patient-specific velocity profiles at peak systolic flow rate were extracted using MEVISFlow (v. 10.3, Fraunhofer MEVIS, Bremen, Germany) and set as inlet boundary conditions. The used CFD pipeline was earlier validated by a comparison with 4D VEC MRI measured velocity fields as well as clinically validated against catheter measured pressure drops in cases of CoA [27].

3.2 Statistical analysis

Statistical analysis of the Hodge Decomposition results was done using software package IBM SPSS Statistic, version 25 (IBM, USA). Measured data are presented as mean and standard deviation (SD) for normally distributed data or as a median with IQR. All data were tested for normality using the Kolmogorov-Smirnov-Test. Depending on the results of the normality test, the T-student test or Mann Whitney-U test were used for the group comparison. Paired tests were used to compare pre- and post-treatment results. A p value < 0.05 was considered significant.

4 Results

Results of the HMF-decomposition analysis of 11 CoA patients before and after treatment as well as 10 controls are illustrated in figure 10. The amount of center and Neumann remains small for all three groups. This shows that the choice of boundary condition affects weakly the overall flow in our tested cases. The T-student test found significantly lower gradient and significantly higher Dirichlet in CoA cases before treatment vs. controls: 0.3 (SD=0.083) vs. 0.46 (SD=0.065) gradient, and 0.54 (SD=0.125) vs. 0.42 (SD=0.065) Dirichlet. The co-gradient in the CoA group was higher as in controls with median 0.119 IQR [0.069-0.147]

vs. median 0.086 IQR [0.065-0.098], approaching significance (Mann-Whitney test, $p=0.061$). Overall significant reduction (paired Wilcoxon test, $p=0.041$) in co-gradient has been observed from pre (median 0.119 IQR [0.069-0.147]) to post intervention (median 0.070 IQR [0.064-0.113]) as expected from the theoretical experimentation exposed previously. However, no significant changes in the major flow descriptors of gradient ($p=0.174$) and Dirichlet ($p=0.073$) were found between pre and post treatment WSS vector fields (paired T-Student test).

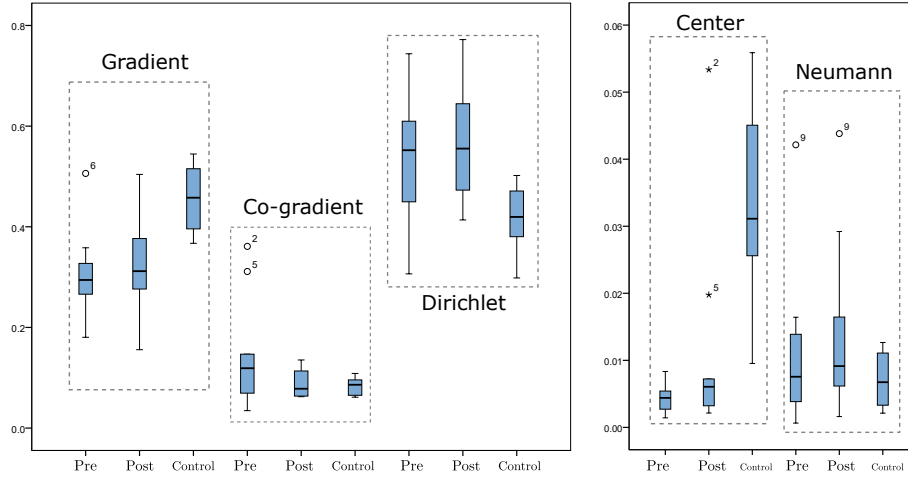


Figure 10: Comparison of the WSS of 11 patients before and after intervention, and 10 healthy patients. An improvement in gradient and Dirichlet while reduction in co-gradient is observed.

5 Discussion

Our first results on the application of a discrete HMF-decomposition analysis of the aortic flow and especially an analysis of the WSS vector fields of the coarctation of the aorta (congenital narrowing of the aorta) disease revealed great potential of the HMF-decomposition analysis for the computational biofluid mechanics. A statistical analysis of the WSS vector fields for coarctation of the aorta cases before and after the treatment as well as healthy controls found significant differences between disease and control groups, but no significant differences between pre- and post-treatment situations. This means that the disease is not of a local nature characterized by a stenosis itself but affected by a global anatomical shape of the aorta.

We applied the HMF-decomposition first to analyse WSS vector fields, since WSS is a known risk factor for the genesis and progress of pathological processes associated with an interaction between blood flow and vessel wall. The analysis allows for an integral characterization of the WSS distribution. However, it

does not replace an analysis of WSS magnitudes, which are also associated with abnormal blood flow conditions: regions with low WSS promote development of atherosclerosis and thrombus formations, whereas high WSS could cause an injury of endothelial cells. In frames of our study we investigated an impact of side branches, degree of stenosis and/or treatment procedure, inlet flow profile boundary conditions as well as an impact of laminar flow disturbances on WSS vector fields as characterized by the HMF-decomposition. Further possible and planned studies include, for example, an analysis of pulsatile flows, the extension of an analysis to other parts of circulation (e.g. coronary arteries, carotid bifurcations or cerebral vessels) and other diseases (e.g. abdominal aortic aneurysms, cerebral aneurysms or coronary artery disease).

The next stage of our research focuses on a 3D HMF-decomposition. Unlike WSS, Dirichlet and Neumann harmonic flows are zero on models homeomorphic to a ball. This is the case for most biological models. New results on synthetic models have been found in [28], but ignore the flow properties of the vector field, resulting in a three-component decomposition (divergence, curvature and harmonics) for models homeomorphic to a solid ball. A new type of decomposition including a mix-boundary condition would be desirable. However, a decomposition on a surface or 3D volume with boundary $\Omega = \Omega_1 \cup \Omega_2$ producing a harmonic field $\mathcal{H}_{N \cap D}(\Omega_1 \cup \Omega_2)$, where a Neumann boundary condition is applied to Ω_1 and a Dirichlet boundary condition is applied to Ω_2 , is still an open problem. Still, a (non-orthogonal) decomposition for frame-fields (n -symmetric vector fields) has been implicitly introduced in global parameterization methods [29] which will served as our starting point. The introduction of periodic boundary conditions, commonly used in numerical analysis, is also a good strategy to obtain non-zero Neumann and Dirichlet components. This is not complicated for the 2D case. However, it becomes more involved to construct a periodic surface on a 3D volume mesh. Several applications will benefit from this extension, such as denoising of 4D velocity-encoded MRI-generated vector fields or 3D flow visualization of a streamline decomposition.

Summarizing our results, HMF-decomposition is able to support (1) basic research of the flow mediated disease, (2) predictive computational modelling of the treatment procedure as well as (3) quantitative analysis of the hemodynamic treatment outcome. Altogether, it supports a clinical translation of the computational modelling approach.

6 Conclusion

The novel discrete Hodge-Morrey-Friedrichs decomposition was for the first time applied to analyze the WSS vector fields of simulated patient-specific aortic blood flows. The approach seems to be a powerful tool to distinguish pathological and physiologic blood flows, characterize the impact of inflow boundary conditions as well as an impact of a treatment.

Acknowledgement This research was carried out in the framework of MATH-EON supported by the Einstein Foundation Berlin within the ECMath Project CH18.

References

- [1] Yiannis S. Chatzizisis, Ahmet Umit Coskun, Michael Jonas, Elazer R. Edelman, Charles L. Feldman, and Peter H. Stone. Role of endothelial shear stress in the natural history of coronary atherosclerosis and vascular remodeling: Molecular, cellular, and vascular behavior. *Journal of the American College of Cardiology*, 49(25):2379 – 2393, 2007.
- [2] Jeng-Jiann Chiu and Shu Chien. Effects of disturbed flow on vascular endothelium: Pathophysiological basis and clinical perspectives. *Physiological Reviews*, 91(1):327–387, 2011.
- [3] Bo Zhang, Junyi Gu, Ming Qian, Lili Niu, and Dhanjoo Ghista. Study of correlation between wall shear stress and elasticity in atherosclerotic carotid arteries. *BioMedical Engineering OnLine*, 17(1):5, Jan 2018.
- [4] Johannes V. Soulis, Dimitrios K. Fytanidis, Vassilios C. Papaioannou, and George D. Giannoglou. Wall shear stress on ldl accumulation in human reas. *Medical Engineering & Physics*, 32(8):867 – 877, 2010.
- [5] Hui Meng, Zhijie Wang, Yiemeng Hoi, Ling Gao, Eleni Metaxa, Daniel D. Swartz, and John Kolega. Complex hemodynamics at the apex of an arterial bifurcation induces vascular remodeling resembling cerebral aneurysm initiation. 38(6):1924–1931, 2007.
- [6] Loic Boussel, Vitaliy Rayz, Charles McCulloch, Alastair Martin, Gabriel Acevedo-Bolton, Michael Lawton, Randall Higashida, Wade S Smith, William L Young, and David Saloner. Aneurysm growth occurs at region of low wall shear stress patient-specific correlation of hemodynamics and growth in a longitudinal study. 39:2997–3002, 08 2008.
- [7] Raoul R. F. Stevens, Andrii Grytsan, Jacopo Biasetti, Joy Roy, Moritz Lindquist Liljeqvist, and T. Christian Gasser. Biomechanical changes during abdominal aortic aneurysm growth. *PLOS ONE*, 12(11):1–16, 11 2017.
- [8] Neelakantan Saikrishnan, Lucia Mirabella, and Ajit P. Yoganathan. Bicuspid aortic valves are associated with increased wall and turbulence shear stress levels compared to trileaflet aortic valves. *Biomechanics and Modeling in Mechanobiology*, 14(3):577–588, Jun 2015.
- [9] Richard J. Lozowy, David C. S. Kuhn, Annie A. Ducas, and April J. Boyd. The relationship between pulsatile flow impingement and intraluminal thrombus deposition in abdominal aortic aneurysms. *Cardiovascular Engineering and Technology*, 8(1):57–69, Mar 2017.

- [10] Linkai Jing, Jingru Zhong, Jian Liu, Xinjian Yang, Nikhil Paliwal, Hui Meng, Shengzhang Wang, and Ying Zhang. Hemodynamic effect of flow diverter and coils in treatment of large and giant intracranial aneurysms. *World Neurosurgery*, 89:199 – 207, 2016.
- [11] Florian von Knobelsdorff-Brenkenhoff, Ralf F. Trauzeddel, Alex J. Barker, Henriette Gruettner, Michael Markl, and Jeanette Schulz-Menger. Blood flow characteristics in the ascending aorta after aortic valve replacement, a pilot study using 4d-flow mri. *International Journal of Cardiology*, 170(3):426 – 433, 2014.
- [12] Amirhossein Arzani and Shawn C. Shadden. Wall shear stress fixed points in cardiovascular fluid mechanics. *Journal of Biomechanics*, 73:145 – 152, 2018.
- [13] Leonid Goubergrits, Jens Schaller, Ulrich Kertzscher, Thies Woelken, Moritz Ringelstein, and Andreas Spuler. Hemodynamic impact of cerebral aneurysm endovascular treatment devices: coils and flow diverters. *Expert Review of Medical Devices*, 11(4):361–373, 2014.
- [14] Paul D Morris, Andrew Narracott, Hendrik von Tengg-Kobligk, Daniel Alejandro Silva Soto, Sarah Hsiao, Angela Lungu, Paul Evans, Neil W Bressloff, Patricia V Lawford, D Rodney Hose, and Julian P Gunn. Computational fluid dynamics modelling in cardiovascular medicine. *Heart*, 2015.
- [15] Jose Fernando Rodriguez-Palomares, Lydia Dux-Santoy, Andrea Guala, Raquel Kale, Giuliana Maldonado, Gisela Teixidó-Turà, Laura Galian, Marina Huguet, Filipa Valente, Laura Gutiérrez, Teresa González-Alujas, Kevin M. Johnson, Oliver Wieben, David García-Dorado, and Arturo Evangelista. Aortic flow patterns and wall shear stress maps by 4d-flow cardiovascular magnetic resonance in the assessment of aortic dilatation in bicuspid aortic valve disease. *Journal of Cardiovascular Magnetic Resonance*, 20(1):28, Apr 2018.
- [16] Sujata Prakash and C Ethier. Requirements for mesh resolution in 3d computational hemodynamics. 123:134–44, 05 2001.
- [17] G. Schwarz. *Hodge decomposition: a method for solving boundary value problems*. Lecture notes in mathematics. Springer, 1995.
- [18] H. Bhatia, G. Norgard, V. Pascucci, and P. Bremer. The Helmholtz-Hodge decomposition - a survey. *IEEE Transactions on Visualization and Computer Graphics*, 19(8):1386–1404, 2013.
- [19] C. Shonkwiler. Poincaré duality angles and the Dirichlet-to-Neumann operator. *Inverse Problems*, 29(4), 2013.
- [20] K. Poelke and K. Polthier. Boundary-aware hodge decompositions for piecewise constant vector fields. *Computer-Aided Design*, 78:126 – 136, 2016.

- [21] K. Polthier and E. Preuss. Identifying vector field singularities using a discrete Hodge decomposition. In Hans-Christian Hege and Konrad Polthier, editors, *Visualization and Mathematics III*, pages 113–134. Springer Verlag, 2003.
- [22] M. Wardetzky. *Discrete Differential Operators on Polyhedral Surfaces - Convergence and Approximation*. PhD thesis, Freie Universität Berlin, 2006.
- [23] O. Azencot, M. Ovsjanikov, F. Chazal, and M. Ben-Chen. Discrete derivatives of vector fields on surfaces—an operator approach. *ACM Transactions on Graphics (TOG)*, 34(3):29, 2015.
- [24] Konstantin Poelke and Konrad Polthier. Boundary-aware hodge decompositions for piecewise constant vector fields. *Computer-Aided Design*, 78:126 – 136, 2016. {SPM} 2016.
- [25] Hellmeier Florian, Nordmeyer Sarah, Yevtushenko Pavlo, Bruening Jan, Berger Felix, Kuehne Titus, Goubergrits Leonid, and Kelm Marcus. Hemodynamic evaluation of a biological and mechanical aortic valve prosthesis using patient-specific mri-based cfd. *Artificial Organs*, 42(1):49–57, 2017.
- [26] Safoora Karimi, Mahsa Dabagh, Paritosh Vasava, Mitra Dadvar, Bahram Dabir, and Payman Jalali. Effect of rheological models on the hemodynamics within human aorta: Cfd study on ct image-based geometry. *Journal of Non-Newtonian Fluid Mechanics*, 207:42 – 52, 2014.
- [27] Goubergrits Leonid, Riesenkampff Eugenie, Yevtushenko Pavlo, Schaller Jens, Kertzschel Ulrich, Hennemuth Anja, Berger Felix, Schubert Stephan, and Kuehne Titus. Mri-based computational fluid dynamics for diagnosis and treatment prediction: Clinical validation study in patients with coarctation of aorta. *Journal of Magnetic Resonance Imaging*, 41(4):909–916, 2015.
- [28] Konstantin Poelke. *Hodge-Type Decompositions for Piecewise Constant Vector Fields on Simplicial Surfaces and Solids with Boundary*. PhD thesis, Freie Universität Berlin, 2017.
- [29] D. Bommers, H. Zimmer, and L. Kobbelt. Mixed-integer quadrangulation. *ACM Trans. Graph.*, 28(3):77:1–77:10, July 2009.